

Seismic events extraction method based on the B-COSFIRE filter combined with the differential evolution algorithm.

ZHAO, J., LI, Y., LEI, H., REN, J., ZHANG, F. and SHEN, H.

2024

This version of the article has been accepted for publication, after peer review (when applicable) and is subject to Springer Nature's [AM terms of use](#), but is not the Version of Record and does not reflect post-acceptance improvements, or any corrections. The Version of Record is available online at: <https://doi.org/10.1007/s11600-023-01222-1>

Seismic events extraction method based on the B-COSFIRE filter combined with the differential evolution algorithm

Jing Zhao¹ Yang Li¹ Haojie Lei¹ Jinchang Ren² Fuku Zhang¹ Hongyan Shen¹

¹ School of Earth Science and Engineering, Xi'an Shiyou University, Xi'an, China

² National Subsea Centre, Robert Gordon University, Aberdeen, UK

Abstract

Based on an analysis of the information processing mechanism in the primary visual cortex of biological vision, this study proposes an integration method of bar-combination of shifted filter responses (B-COSFIRE) filter with the differential evolution (DE) algorithm for enhancing the precision of events extraction. First, the B-COSFIRE filter incorporates trainable and unsupervised features, utilizing the two-dimensional expression of the difference-of-Gaussians (DoG) model to simulate the receptive field model. By capitalizing on the blur and shift properties of the DoG response, the proposed approach enhances the continuous effective signal while attenuating discontinuous noise signal, thereby demonstrating superior noise robustness compared to conventional methods. Second, the selectivity of proposed filter is not predefined during the implementation but automatically determined based on the given prototype pattern during the configuration process, resulting in a universal solution adaptable to various target patterns. Lastly, we employ the DE algorithm to optimize the feature selection process, enabling the extraction of a minimum feature subset that maximizes the performance of events characterization. The B-COSFIRE method is widely used in the field of image processing. When applying it to seismic exploration, the seismic data used by this algorithm is in 'sgy' format, providing richer information than traditional image data. The proposed model can effectively detect the event in seismic data with significant data volume and substantial noise interference. The B-COSFIRE filter method outperforms conventional edge detection techniques by accurately capturing seismic events of varying widths, aligning with the principles observed in biological vision mechanisms. The extracted events exhibit enhanced continuity and accuracy compared to existing approaches.

Keywords Events extraction · B-COSFIRE filter · The differential evolution algorithm · Biological vision · The DoG model

Introduction

During the propagation of seismic wave, when they encounter rock interfaces characterized by varying medium properties, a portion of the energy is reflected back to the surface. During the propagation of seismic waves, when the waves encounter rock interfaces with different media properties, a portion of the energy will be reflected back to the surface and detected by the receivers, with each record corresponding to a specific geophone. As seismic waves are reflected by multiple interfaces, each trace of the seismic signal generates multiple reflection seismic wavelets. These wavelets manifest as distinct vibrational profiles, with the line connecting the extreme values (commonly referred to as peaks or troughs) of the vibrational profile's phase on the seismic record presenting an event (Li 2015). Most information obtained in seismic exploration is included in these events, making it crucial to determine how to extract their visual features effectively (Zhao 2005). For instance, the self-shoot time of events provides partial insight into the depth of the interface, and the shape of the events represents the velocity of seismic wave within the medium. In seismic data processing and interpretation, the structural interpretation of the stratum profile, along with the description of the positions of seismic image detection point, constitutes a crucial component of the seismic profile's structural interpretation.

The visual cognition in seismic data processing refers to the interpretation and understanding of seismic data using visual perception and cognitive processes. It involves the analysis of seismic profiles, waveforms, and various data representations to extract meaningful information about subsurface structures, geological features, and potential hydrocarbon reservoirs. Visual cognition allows geoscientists and seismic interpreters to visually identify patterns, anomalies, and seismic characteristics that may indicate geological formations or potential hydrocarbon prospects. The visual cognition in seismic data processing enables the events extraction of the seismic reflection profile influenced by stratum structure. Consequently, the visual information derived from the seismic section's events can be harnessed to determine the position of effective oil/gas in the seismic section. This stratigraphic information, in turn, facilitates the processing and interpretation of seismic data, thereby enhancing the efficiency of seismic exploration. (Lu 1993). The seismic wavelet variation of events is caused by complex mechanisms, such as the seismic wave propagation, anomalies, anisotropy, and attenuation. Consequently, events contain substantial information about subsurface geological characteristics. Hence, the detection and pickup of events are indispensable for effective processing and interpretation of seismic data.

To extract event information from seismic data, various detection techniques have been developed for seismic exploration. Among these techniques, the following three methods are most representative.

- (1) Edge detection method (Li 2007): The method entails the conversion of the amplitude value of each sampling point in a two-dimensional seismic record into different gray values, treating the seismic gather as a gray image. Subsequently, edge detection method used in image processing can detect events within the gray image. However, the information extracted using the edge detection method tends to be fuzzy, with the resolution being significantly disturbed by spatial and frequency interference, as well as the influence of noise factors. The detection result represents the envelope of the gray mutation region, leading to a notably low resolution; thus, it is not directly suitable for use as the definitive events detection results (Xiong 2009; Ning 2005).
- (2) Neural network method (McComack 1993; Glinsky 1991): The method uses known events as standard samples to simulate a neural network, wherein the connection weights between neurons are gradually adjusted using the error backpropagation method. The neural network method requires an adequate number of samples for effective training. However, the selection of appropriate samples is challenging. Introducing new samples can also affect the neural network performance, and the numerous iterative operations required for training can result in prolonged processing time (Wang 2018; Bondar 1992; Ma et al. 2023).
- (3) Cross-correlation method (Spagnolini 1991; Ding 2012): The method relies on the fundamental principle of utilizing the waveform similarity features of events across seismic traces to extract events susceptible to noise. The spatial resolution decreases with an increasing number of calculation traces, which leads to a larger computational workload.
- (4) Chain matching method: The method represents each waveform by identifying peaks and troughs with multiple features, which are subsequently linked together. The task of events extraction is then transformed into a best matching problem between chains, i.e., finding the minimum link path. This method is also disturbed by noise, space, and frequency, making it difficult to solve complex events processing problems (Haralick 1984).

Additionally, Tu et al. (1993) proposed an automatic events extraction system. This method consists of three steps: a two-dimensional (2D) matched filter, a Kalman filter, and a flexible template. Matched filtering is used to detect targets, while the Kalman filter eliminates random interference and recovers data from noise. Waveform correlation-based detection methods can yield effective results, particularly when the separation between the main event and the target event is smaller than the dominant wavelength (Gibbons and Ringdal 2006a, b; Michelet and Toksöz 2007; Arrowsmith and Eisner 2006). Song et al. (2010); Song and Toksöz (2011) applied the correlation-based weak event detection method to microseismic events caused by hydraulic fracturing. Yangkang Chen (2020) presents a concept of microseismic event detection method based on unsupervised machine learning. Zhou (2019) introduces a hybrid event detection and phase-picking algorithm utilizing a two-layer bidirectional RNN to pick P- and S-arrival times. Liu (2022) proposes a microseismic first-arrival picking method using fine-tuning feature pyramid networks.

In the domain of seismic data processing, improving the efficiency of seismic exploration requires obtaining the precise determination of position of effective oil and gas in the stratigraphic horizon, achieved through events extraction from the seismic profile. Then, processing and interpretation of seismic data can be achieved using the effective stratigraphic information. The simulation of the intricate biological visual recognition mechanism for achieving the extraction of target contours from seismic data presents an integration of seismic exploration with artificial intelligence. This interdisciplinary endeavor represents a challenging and vibrant frontier of ongoing research efforts, attracting significant attention in the scientific community.

The B-COSFIRE filter method, initially designed for retinal blood vessels delineation (Azzopardi and Petkov 2012), is based on the combination of receptive fields (CORF) computational model of a simple cell in the visual cortex and its implementation called combination of shifted filter responses (COSFIRE) (Azzopardi and Petkov 2013). The versatility of this filter has also been demonstrated in the analysis of computed tomography angiography (CTA) images (Zhu 2015), showcasing its suitability for extracting and segmenting various slender structures. In the proposed method, a 2D representation of the difference of double-Gaussian (DoG) model is used to simulate the receptive field model of optic ganglion cell, enabling the central region of the receptive field to have excitatory (positive) and inhibitory domains with inhibitory surroundings (negative). The DoG response is further manipulated through blurring and shifting, and the resulting B-COSFIRE filter response model is obtained by calculating its weighted geometric average (Strisciuglio 2016, 2017; Azzopardi and Petkov 2013; Azzo-pardi et al. 2015; Lara et al. 2019).

This paper presents a novel approach utilizing a set of B-COSFIRE filters to address the event picking problem in seismic data, specifically focusing on slender structures. These filters are capable of selecting events with varying widths. The methodology begins with the preprocessing of seismic data, involving the wavelet fusion of the instantaneous frequency of the envelope peak and the instantaneous amplitude of the slant stack peak of the pre-stack seismic data. Then, the principles of the B-COSFIRE filter and the feature selection process based on the DE algorithm are introduced. The study combines the responses of two B-COSFIRE filters: one for detecting events and the other for detecting the end of events. The selection of parameters for the end-events filter is dependent on maximizing the performance of both filters, with the configuration rely-ing on the events filter. The choice of filter parameters is crucial, and the configuration parameters for each filter are selected to optimize performance across all common widths of the bar structure. Subsets of the B-COSFIRE filters are determined using information theory and machine learning techniques, allowing for the selection of bar structures with different widths. The impact of system performance is evaluated by employing the DE algorithm as a feature selection method. The DE algorithm (Zhao 2019, 2012; Wang and Gao 2012, 2010a, b) is used to construct the feature vector based on the response of the B-COSFIRE filter, aiming to obtain the minimum feature subset that maximizes event description performance. This approach enables the evaluation of the combined contribution of multiple features and exploration of a larger solution space. The proposed model can effectively detect the event edge of the seismic data target contour with a large volume of data and various noise interferences. Compared to other traditional edge detection methods, the B-COSFIRE filter demonstrates the ability to pick up seismic data events with different widths, aligning more closely with the biological vision mechanism. The events picked up by this method exhibit higher continuity and accuracy compared to existing approaches.

Method

The following is the flowchart of the proposed algorithm (Fig. 1).

Preprocessing of the seismic data

The preprocessing aims to enhance the signal-to-noise ratio (SNR) of pre-stack seismic data, leading to improved data quality. Events pickup is carried out using both pre-stack and post-stack seismic data. Pre-stack seismic data contain more information than post-stack seismic data. By avoiding processes such as NMO stretching and stacking, the amplitude and frequency information remains undamaged and enables the reflection of some fine formation characteristics. However, the disadvantage of higher noise level has always puzzled the researchers. Therefore, considering the low signal-to-noise ratio of pre-stack seismic data, we propose a high-precision events extraction method. In the following section, we provide a concise overview of the pre-processing procedure. Assume that the source wavelet can be approximated by the following constant phase wavelet with four parameters (Gao 2011; Zhao 2013):

$$s(0, t) = A' \left(\frac{\delta^2}{\pi} \right)^{1/4} \exp[i(\sigma t + \phi) - (\delta t)^2 / 2], \quad (1)$$

where σ is the modulated angular frequency, δ is the energy attenuation factor, A' and ϕ are the amplitude and the phase, respectively.

The EPIF (envelope peak instantaneous frequency) of the zero-time source wavelet is obtained by (Gao 2011):

$$f_p(0) = \frac{\sigma}{2\pi} + \frac{\frac{\delta^2}{2\pi^2} \exp \left[-\frac{2\pi^2}{\delta^2} \left(\frac{\sigma}{2\pi} \right)^2 \right]}{\int_0^\infty \exp \left[-\frac{2\pi^2}{\delta^2} \left(f - \frac{\sigma}{2\pi} \right)^2 \right] df}. \quad (2)$$

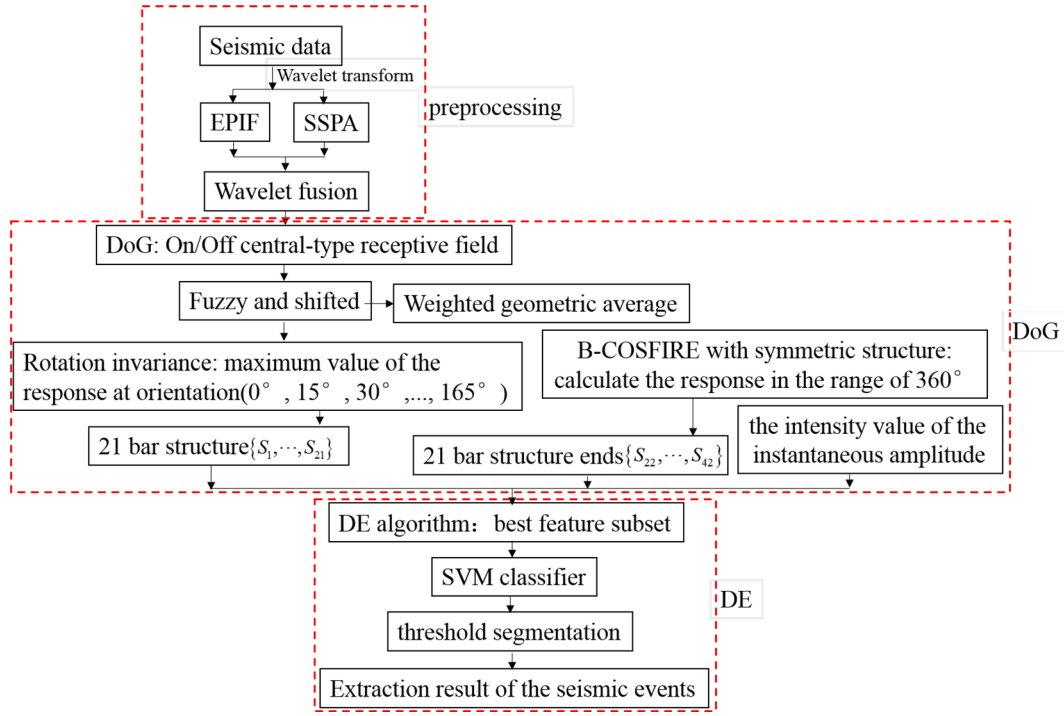
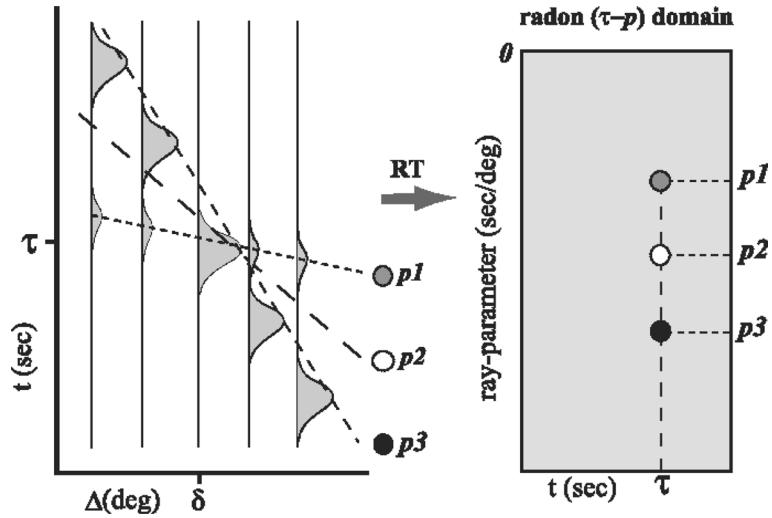


Fig. 1 The flow chart of the proposed algorithm

Fig. 2 Schematic representation of the Radon transformation(Schultz and Yu Jeffrey 2013)



The calculation process of the slant stack peak amplitude (SSPA) profile is as follows (Zhao 2019). Figure 2 is the local linear Radon transform diagram. For a selected reference trace on the instantaneous amplitude section, τ_j denotes a certain time intercept, where several traces near the reference trace are superimposed along n_p straight lines with different slopes $p_j(j = 1, 2, \dots, n_p)$ (slope in interval sampling Δp). The sum of the instantaneous amplitude along different directions at the time intercept is recorded at the corresponding position (τ_j, p_j) of the coordinate axis $\tau - p$. When the selected stacking slope closely or equals to the slope of the events, the data in the time-distance $(t-x)$ domain exhibit maximum value. By averaging the maximum stacking values and placing them at the corresponding position (τ_j, x_m) in the $t-x$ domain, a super-gather can be constructed to increase the SNR, which is called the slant stack peak amplitude (SSPA) profile.

So far, the EPIF profile and the SSPA profile have been obtained. Next, we calculate the wavelet fusion of these two profiles.

Trainable COSFIRE filter

The combination of shifted filter responses (COSFIRE) is an unsupervised pattern detection method in computer vision (Badawi and Fraz 2018). Similar to deep learning methodologies, the COSFIRE approach avoids the need of engineering hand-crafted features and instead learns to determine important features directly from prototype training patterns. The automatic learning of suitable data representations allows the construction of flexible and adaptive pattern recognition systems (Strisciuglio and Petkov 2017). In particular, Azzopardi and Petkov (2013) demonstrated the effectiveness of COSFIRE filters in detecting vascular bifurcations in retinal fundus images (Azzopardi and Petkov 2012). By using a collection of center-off and centeron DoG filters, we can effectively configure a contour operator. The COSFIRE method can be classified as a combination of shifted filter responses, key point detection, and pattern recognition. It functions as a trainable filter and combines the responses from a group of DoG filters.

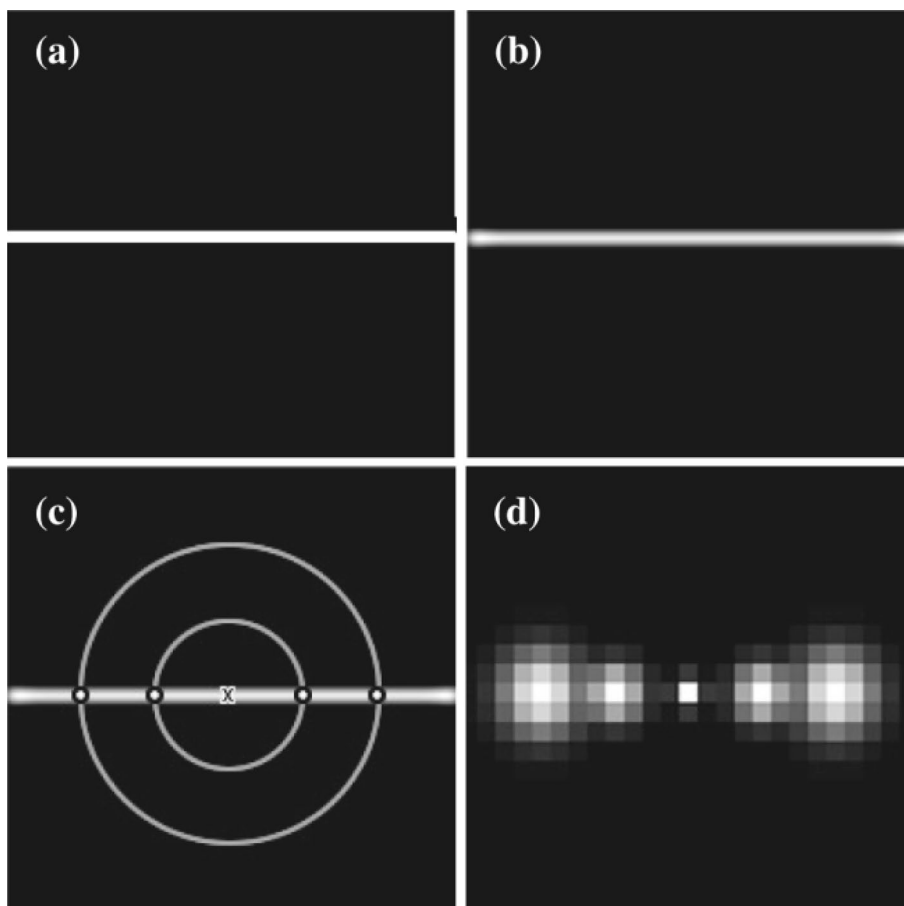
Trainable B-COSFIRE filter

We apply B-COSFIRE filtering to the wavelet fusion pro-file due to the higher SNR of preprocessed seismic data. A B-COSFIRE filter is derived from the existing COSFIRE approach; it achieves orientation selectivity by computing the weighted geometric mean of the output of a pool of DoG filters, whose supports are aligned in a collinear manner.

The human visual nervous system has evolved to receive and cognize external scenes with extremely high resolution. When the eyes receive light stimulation and excitation, gan-glion cells transmit sensory information to the central nervous system, and their response area is called the classical receptive field. The classical receptive field exhibits a concentric circle structure where the center and periphery have antagonistic effects, which can be described by the DoG model. Figure 3a shows the configuration of the B-COSFIRE filter as a horizontal bar, representing the response of the input central DoG filter at a specific position within the support area. Figure 3b shows the response of the DoG filter, and Fig. 3c shows the local maximum DoG response of the concentric circle along the target point (identified by the cross mark in the center). Figure 3d depicts the final filter, with the size of the spots corresponding to the standard deviation of the Gaussian blur function. The blurring operation calculates the DoG maximum weighted response to improve the robustness.

Fig.3 An example of a B-COSFIRE filter configuration using a horizontally synthesized bar structure. **a** Schematic diagram of the B-COSFIRE filter.

b Response of the DoG filter; **c** Local maximum DoG response along the concentric circles of the target point; **d** Sketch of the final filter



The key advantage of B-COSFIRE filters lies in their trainability nature, allowing for automatic configuration of the optimal filter parameters according to the target and leading to the best pickup results. It means that, unlike predefined selectivity in the filter implementation, the selectivity is determined by userdefined prototype patterns (such as straight containers, forks, or intersections) during automatic configuration. The 1D expression of the DoG model is given as follows (Strisciuglio 2016):

$$\text{DoG}_{\sigma_1\sigma_2A_1A_2}(x) = \frac{A_1}{\sqrt{2\pi}\sigma_1} \exp\left(-\frac{x^2}{2\sigma_1^2}\right) - \frac{A_2}{\sqrt{2\pi}\sigma_2} \exp\left(-\frac{x^2}{2\sigma_2^2}\right), \quad (3)$$

where A_1, A_2 represent the sensitivity of the central excitatory domain and its surrounding inhibitory domain, respectively, σ_1 is the mean square deviation of the Gaussian function in the central domain, and σ_2 is the mean square deviation of the Gaussian function in the inhibitory domain. The DoG response is blurred and shifted, and its weighted geometric average is computed to generate the output of the B-COSFIRE filter. Two sets of B-COSFIRE filters are established, and the responses of these two sets of filters are combined for seismic data event pickup. In the two sets of B-COSFIRE filters, one group is dedicated to detecting the events, while the other focuses on detecting the end of the events. Next, the B-COSFIRE filter is obtained. COSFIRE is a combination of shifted filter response models. Referred to as B-COSFIRE, this approach incorporates the selection of bar structures, exhibiting sensitivity to changes in direction and demonstrating strong resistance and adaptability in the presence of rotation and shape variations. The B-COSFIRE filter proposed in this paper is nonlinear, and its nonlinear response realizes directional selectivity by multiplying the output from a set of DoG filters with colinear alignment. The filter tolerates changes in rotation and slight deformations. To simulate the receptive field model, a 2D expression of the DoG model is given, which can realize the function of the central region with excitability (positive) and inhibitory domains with inhibitory surroundings (negative):

$$\text{DoG}_\sigma^+(x, y) = \frac{1}{2\pi\sigma^2} \exp\left(-\frac{x^2+y^2}{2\sigma^2}\right) - \frac{1}{2\pi(0.5\sigma)^2} \exp\left(-\frac{x^2+y^2}{2(0.5\sigma)^2}\right). \quad (4)$$

Motivated by electrophysiological studies of LGN cells in owl monkeys (Irvine et al. 1993; Xu et al. 2002), the corresponding value of the central excitatory domain is set as 0.5σ , where σ is the spatial distribution degree of the Gaussian function (i.e., the standard deviation) of the surrounding inhibitory domain. The relationship between the value of and the peak of the Gaussian function is illustrated in Fig. 4. A smaller value of σ leads to a higher peak in the Gaussian function, while a larger value results in a smoother peak and a more blurred and smoothed image convolution output. This function is a recognized calculation model for some cells in the lateral geniculate nucleus (LGN) of the brain (Rodieck 1965). As shown in Fig. 5, on the left is the original figure and the Gaussian blur of three different sigma values. On the right is the difference graph (DOG for short) of the three Gaussian functions, obtained by successively subtracting the images after Gaussian filtering (in adjacent states) in pairs. The red mark is the current pixel point, and the corresponding yellow mark represents the adjacent point of the current pixel point. There are 26 (27 yellow points minus one red point in the figure below). If this point (red point) is the maximum or minimum value of all adjacent pixel points (yellow point), then the corresponding red mark is considered as a feature point.

$\text{DoG}_\sigma^+(x, y)$ is the ON central-type receptive field, where the center is the excitatory domain, and the periphery is the inhibitory domain. $\text{DoG}_\sigma^-(x, y)$ is the OFF center-type receptive field, which is defined as:

$$\text{DoG}_\sigma^-(x, y) = -\text{DoG}_\sigma^+(x, y). \quad (5)$$

The above DoG model can simulate the concentric antagonistic structure of the cells.

For a given location (x, y) and intensity distribution $I(x', y')$ of the seismic data I , the response of the DoG can be calculated as follows:

$$c_\sigma(x, y) \stackrel{\text{def}}{=} |I * \text{DoG}_\sigma|^+, \quad (6)$$

where $*$ is the convolution and $|\cdot|^+$ is the half-wave rectification. We then consider the DoG responses along a concentric circle around a given point of interest, selecting the DoG with a local maximum from those responses.

Fig. 4 The 2D Gaussian function

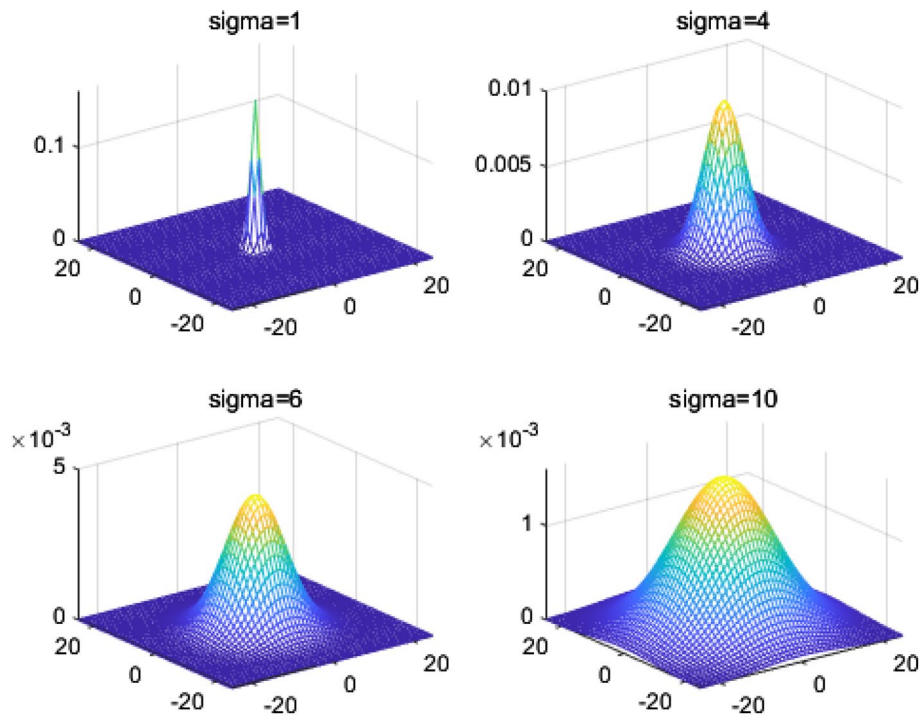


Fig. 5 The work principle of the 2D DoG

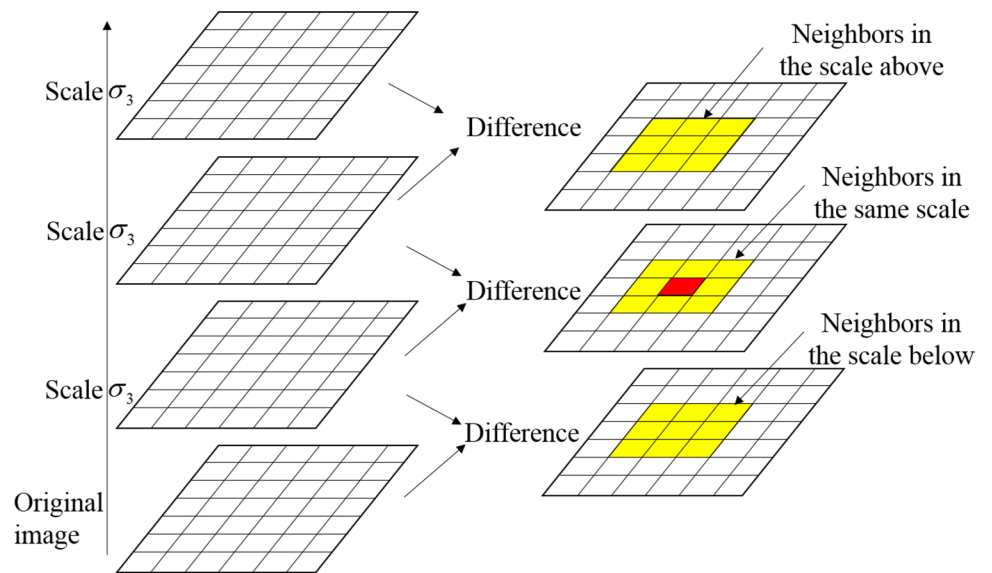
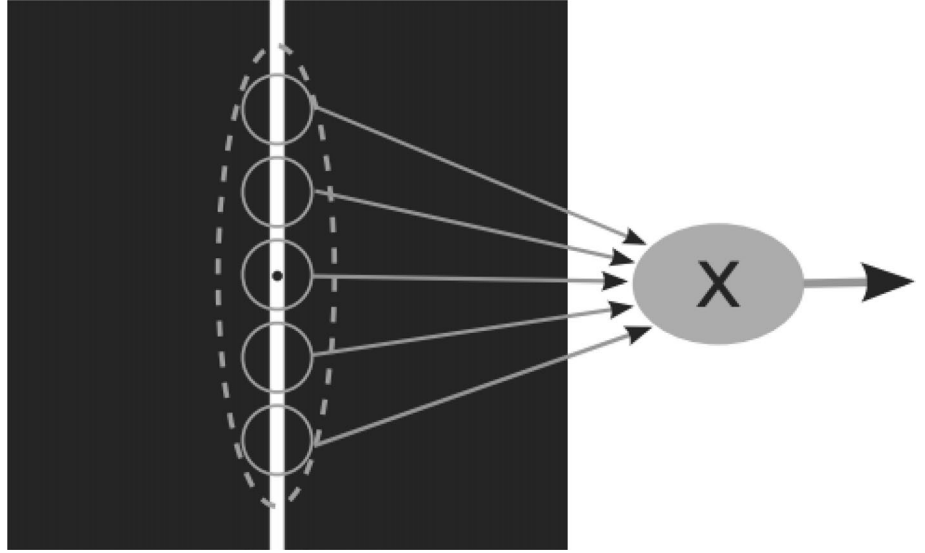


Fig. 6 Schematic diagram of the B-COSFIRE filter



The direction of B-COSFIRE is chosen to be the same as that of the stripe tissue. We describe the i th point with three parameters σ_i , ρ_i and ϕ_i ; σ_i is the standard deviation of the DoG filter, (ρ_i, ϕ_i) is the polar coordinate that represents its position. Using the DoG model with the predefined σ , and the specified point is taken as the center of the circle to analyze the response $c_\sigma(x, y)$ within the range of N concentric circles. Figure 6 illustrates the configuration of the B-COSFIRE filtering combination, taking into account the seismic data's event characteristics. The center of the light gray circle corresponds to the center point of the B-COSFIRE filtering combination, and the black point, which arises from the intersection of the middle vertical line and the concentric circle, represents the extreme point of the DoG response. The parameters of filtering combination are:

$$S = \{(\sigma_i, \rho_i, \phi_i) | i = 1, \dots, n\}, \quad (7)$$

where S defines a B-COSFIRE filter with a selective preference for a given prototype and n is the number of the DoG filters to be configured. The values used in the following equation correspond to the analysis of the vertical line depicted in Fig. 3c and are determined through automatic analysis of the corresponding input pattern. The values for ρ and ϕ are obtained through automatic analysis and generation based on the points mentioned earlier:

$$S = \left\{ \begin{array}{l} (\sigma_1 = 2.6, \rho_1 = 0, \phi_1 = 0), \\ (\sigma_2 = 2.6, \rho_2 = 2, \phi_2 = 1.57), \\ (\sigma_3 = 2.6, \rho_3 = 2, \phi_3 = 4.71), \\ (\sigma_4 = 2.6, \rho_4 = 4, \phi_4 = 1.57), \\ (\sigma_5 = 2.6, \rho_5 = 4, \phi_5 = 4.71) \end{array} \right\}. \quad (8)$$

The initial step involves convolving the input images with the difference of Gaussian (DoG) function, which is characterized by a predefined standard deviation specified in the tuples of the set S .

The next step involves applying the blurring shift operation to the DoG filter in order to accommodate potential errors in the priority positions of relevant points. As depicted in Fig. 3d, the DoG 3D function is multi-scale, resulting in varying blob shapes. At the center point of the horizontally oriented bar, the mean square deviation of the DoG filter is the minimized, leading to the highest peak of the Gaussian function. As we move away from the center point, the mean square deviation of the DoG filter increases, resulting in smoother Gaussian peaks and reduced impact of blurring and shift operations. The mean square deviations σ_1 and σ_2 determine the image's blurriness. The mean square deviation, represented by σ , determines the level of blurriness in the image. A larger σ value indicates a greater degree of blurriness, while a smaller σ value captures more detailed information. The blurring operation calculates the maximum value of the weighted threshold response of a DoG filter. The maximum DoG response in the

local neighborhood of the maximum weighted DoG response $G_{\sigma'}(x', y')$ is computed by the blurring operation to improve its fault tolerance. The weight is obtained by multiplying the coefficient of the DoG filter response with the Gaussian function $c_{\sigma'}(x', y')$, where the standard deviation σ' is a linear function of the distance ρ_i from the filter support center:

from the filter support center: $\sigma' = \sigma'_0 + \alpha \rho_i$. The values of σ'_0 and α are constants that can be adjusted based on the specific application requirements. ρ_i represents the distance between the filter support center and the priority position of the correlation point.

In order to refine the alignment of the blurring DoG responses, this paper introduces a vector-based approach. Each blurring DoG response is shifted towards the center of the support region using a displacement vector of length ρ_i , which is the complementary angle of ϕ_i ; the associated change vector is $(\Delta x_i, \Delta y_i)$, $\Delta x_i = \tau \cos \phi_i$, and $\Delta y_i = -\rho_i \sin \phi_i$. We calculate the fuzziness of the tuples σ_i, ρ_i, ϕ_i and the response of DoG in the inverse direction of ϕ_i and shift it, as shown in the equation below:

$$s_{\sigma_i, \rho_i, \phi_i}(x, y) = \max_{x', y'} \left\{ c_{\sigma_i}(x - \Delta x_i - x', y - \Delta y_i - y') G_{\sigma'}(x', y') \right\}, \quad (9)$$

where $-3\sigma' \leq x', y' \leq 3\sigma'$.

Next, the B-COSFIRE filter response model is calculated. The B-COSFIRE filter output response $r_s(x, y)$ is the weighted geometric average of all blurry and shifted DoG responses in the corresponding tuple S :

$$r_s(x, y) \stackrel{\text{def}}{=} \left| \left(\prod_{i=1}^{|S|} (s_{\sigma_i, \rho_i, \phi_i}(x, y))^{\omega_i} \right)^{1/\sum_{i=1}^{|S|} \omega_i} \right|_{\tau}, \quad (10)$$

where $\omega_i = \exp^{-\frac{\rho_i^2}{2\hat{\sigma}^2}}$, $\hat{\sigma} = \frac{1}{3} \max_{i \in \{1, \dots, |S|\}} \{\rho_i\}$, (ρ_i, ϕ_i) is the polar coordinate of the i th DoG response with respect to the center of the filter support, $|\cdot|_{\tau}$ is the response threshold representing the maximum response at the fraction τ ($0 \leq \tau \leq 1$). The weighted geometric mean is an “and” type function, meaning that a B-COSFIRE filter can only produce a response if all fuzziness and shift responses $s_{\sigma_i, \rho_i, \phi_i}(x, y)$ are greater than zero. The contribution of blurring and shift response decreases with increasing distance from the support center of the B-COSFIRE filter.

The above equations configure a B-COSFIRE filter, which can be used for horizontally oriented containers. To achieve multi-directional selectivity, multiple B-COSFIRE filters can be configured by using prototype patterns with different orientations. The weighted geometric average is an “and” function, where the response value is obtained only when all the individual responses meet the condition “> 0.” It is noteworthy that the influence of blurring and shift operations decreases as the specified point moves farther away from the filter’s center. It can be seen that we should first set the bar direction for the filter. By manipulating the parameters ψ associated with each tuple, a new set $R_{\psi}(S)$ is created. Here, we integrate the set S and add the $R_{\psi}(S)$ to achieve rotation invariance:

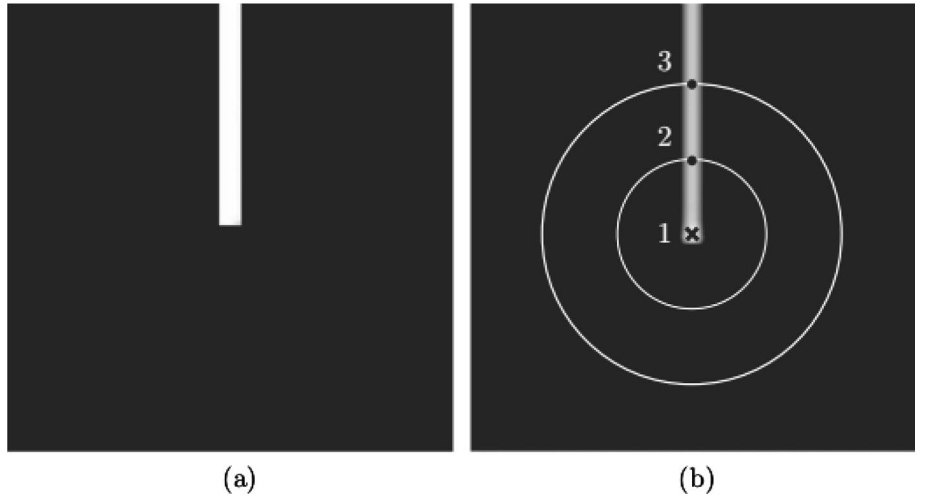
$$R_{\psi}(S) = (\sigma_i, \rho_i, \phi_i + \psi | \forall (\sigma_i, \rho_i, \phi_i) \in S). \quad (11)$$

The above equation represents a B-COSFIRE filter with an orientation preference of radians ψ , offset from the orientation preference of the original filter S . It can track bar targets in all directions, sum all the responses obtained, and calculate the response values of each pixel at different orientations ($0^\circ, 15^\circ, 30^\circ, \dots, 165^\circ$), and then the maximum value is selected as the feature of this point. In this paper, a set of B-COSFIRE filters with diverse orientation preferences is selected, which can be expressed as:

$$r_S(x, y) = \max_{\psi \in \Psi} \left\{ r_{R_{\psi}}(x, y) \right\}, \quad (12)$$

where $\Psi = \left\{ \frac{\pi}{n_r} i | 0 \leq i \leq n_r \right\}$, $n_r = 12$.

Fig. 7 Example of the B-COSFIRE filter configured by using the end of a vertically synthesized bar structure. **a** Prototype of the end of the bar structure; **b** Asymmetric B-COSFIRE filter configured via **(a)**



Due to the discontinuity and asymmetry of seismic data, such as the presence of primary reflection and multiple reflection waves, it is difficult to achieve comprehensive detection when events are picked up. B-COSFIRE operates as a “logical and” function, requiring all inputs to be activated in order to produce a response. Consequently, it faces limitations in generating a response at points of discontinuity. To address this issue, the construction of specific filters for primary reflections and reflected waves is considered. The filters that detect continuous events and direct waves are called B-COSFIRE with symmetric structure, while the filters for discontinuous and reflected waves are called B-COSFIRE with asymmetric structure. Asymmetric structure filters calculate the response in the range of 360° . In practical application, unlike symmetric filters that only calculate the target point on one side, the asymmetric structure filters need to double the number of azimuths to obtain the endpoints of the bar structure in all directions. The target points can be located in any direction. As shown in Fig. 7, the center of the concentric circles is the response center of the filter, and the black dots represent the response extreme values. A new B-COSFIRE filter is configured at the end of the bar structure to realize the end response. We utilize a point situated at the end of a bar structure as a notable point. In comparison with the symmetric B-COSFIRE filter, the asymmetric B-COSFIRE filter achieves a more pronounced response at the end of the bar structure.

The width of seismic events, depending on the offset, may range from 1 pixel to several pixels. The larger offset corresponds to greater high-frequency attenuation, increased low frequency, and a broader waveform. Consequently, this paper employs a set of B-COSFIRE filters consisting of 21 bar structures $\{S_1, \dots, S_{21}\}$ and 21 bar structure ends $\{S_{22}, \dots, S_{42}\}$, allowing for the selection of bar structures of varying thicknesses. Large-scale filters exhibit selectivity for wide events and tolerance to background noise, yet they demonstrate minimal response to narrow events. Conversely, small-scale filters have higher selectivity for narrow events but exhibit less tolerance to background noise. The fused responses of these two filter types are anticipated to achieve superior events-extraction performance across various scales. For each event position (x, y) , We construct a pixelation-level feature vector $\mathbf{v}(x, y)$ comprising the responses of the 42 B-COSFIRE filters in the filter bank, in addition to the intensity value $g(x, y)$ of the instantaneous amplitude:

$$\mathbf{v}(x, y) = [g(x, y), r_1(x, y), \dots, r_{42}^T(x, y)], \quad (13)$$

where $r_i(x, y)$ is the rotation tolerance response of the B-COSFIRE filter S_i .

Before classification, this paper applies the inverse hyperbolic sine transformation function to each eigenvector element, reducing data bias and defined as follows:

$$f(v_i, \theta) = \frac{\sinh^{-1}(\theta v_i)}{\theta}. \quad (14)$$

For larger values of v_i and $\theta > 0$, the function operates similarly to a logarithmic transformation. Let $\theta \rightarrow 0$, $f(v_i, \theta) \rightarrow v_i$. The Z-fraction is then calculated to normalize all 43 eigenvalues. This paper applies Z-fraction normalization separately to each image to compensate for lighting variations between images.

The filter library designed above may contain redundant filters. To address this issue, this paper investigates various feature-selection methods to identify a minimal feature subset that can maximize the characterization performance of the events. Ultimately, the differential evolution (DE) algorithm serves as the feature selection method, assessing the impact on system performance, determining the minimum feature subset to optimize event characterization performance, and completing seismic event extraction. We use a training data matrix of size $N \times 43$ as the input, where N represents the number of pixels randomly selected from the training data, and the column number corresponds to the size of the filter bank plus the size of the EPIF (envelope peak instantaneous frequency) data.

The DE algorithm guides the selection of the optimal gene of each subcomponent by employing the local fitness function. Subsequently, it performs the inversion to search for the feature subset with the best performance among numerous possible combinations.

The DE method initially provides a population \mathbf{X} containing M individuals (Wang and Gao 2010a, b, 2012):

$$\mathbf{X} = [\mathbf{x}_1, \mathbf{x}_2, \dots, \mathbf{x}_M]. \quad (15)$$

The k th individual in the population is represented as:

$$\mathbf{x}_k = [x_{k,1}, x_{k,2}, \dots, x_{k,N}], \quad k = 1, \dots, M, \quad (16)$$

where M is the initial number of individuals, which is set according to the actual situation, such as $M = 400$; and N is the dimension of 43 parameters to be estimated (i.e., EPIF and 42 B-COSFIRE filters). The fitness function calculates the average accuracy of the training data and the selected columns. The local fitness function of the k th individual, defined by the L1 norm, is:

$$f_{k,j} = \sum_{l=1}^{\text{NR}} \left| [d_{o,j}(l) - d_{k,j}(l)] \cdot g(l) \right|, \quad (17)$$

where $d_{o,j}(\cdot)$ is the data of the events of the j th column, $d_{k,j}(\cdot)$ is the training data of the j th column calculated by the forward modeling of the k th individual, NR is the trace number of the observed seismic data, and $g(l)$ is the Gaussian window function, defined as follows:

$$g(l) = \exp\left(-\frac{1}{2} \cdot \frac{(l-P)^2}{\sigma'^2}\right), \quad (18)$$

where l is the variable, and σ' is the standard deviation used to control the window's width. The Gaussian window's center is located at the wavelet envelope's peak. For post-stack data, the time window's center should be located at the subcomponent's center, and for prestack data, the time window's center should slide along the hyperbola as the offsets increase. We take the k th individual \mathbf{x}_k as the B-COSFIRE parameter, pick up the position of the seismic events, and calculate a local fitness value for each trace. Then, the local fitness value vector corresponding to the k th individual is:

$$\mathbf{f}_k = [f_{k,1}, f_{k,2}, \dots, f_{k,N}], \quad (19)$$

where the element $f_{k,1}, f_{k,2}, \dots, f_{k,N}$ is the local fitness value of the 1st to N th traces.

Therefore, for a population \mathbf{X} containing M individuals, the local fitness value corresponding to the forward data is an $M \times N$ matrix:

$$\mathbf{f} = \begin{bmatrix} f_{1,1} & f_{1,2} & \dots & f_{1,N} \\ \dots & & & \\ f_{M,1} & f_{M,2} & \dots & f_{M,N} \end{bmatrix}. \quad (20)$$

The initial population \mathbf{X} is also an $M \times N$ matrix.

The DE algorithm employs mutation, crossover, and selection operations to conduct iterative searches. The three main operations are introduced as follows.

Mutation operation: the effective mutation strategy can rapidly improve the genes (parameters to be estimated) within the individual, eventually obtaining the optimal individual after multiple generation iterations. To determine the correct direction of gene mutation, the local fitness function is employed to guide each sub-component's mutation direction in the mutation operation, and a new mutation operator is proposed. We arrange all variables in the j th column of the group \mathbf{X} in ascending sort:

$$\mathbf{x}_{\cdot j}^s = \text{sort}[x_{1j}, x_{2j}, \dots, x_{Mj}] = [x_{1j}^s, x_{2j}^s, \dots, x_{Mj}^s], \quad (21)$$

where the superscript s represents the sorted sequence. The local fitness value of this sequence is:

$$\mathbf{f}_j^s = [f_{1j}^s(x_{1j}^s), f_{2j}^s(x_{2j}^s), \dots, f_{Mj}^s(x_{Mj}^s)]. \quad (22)$$

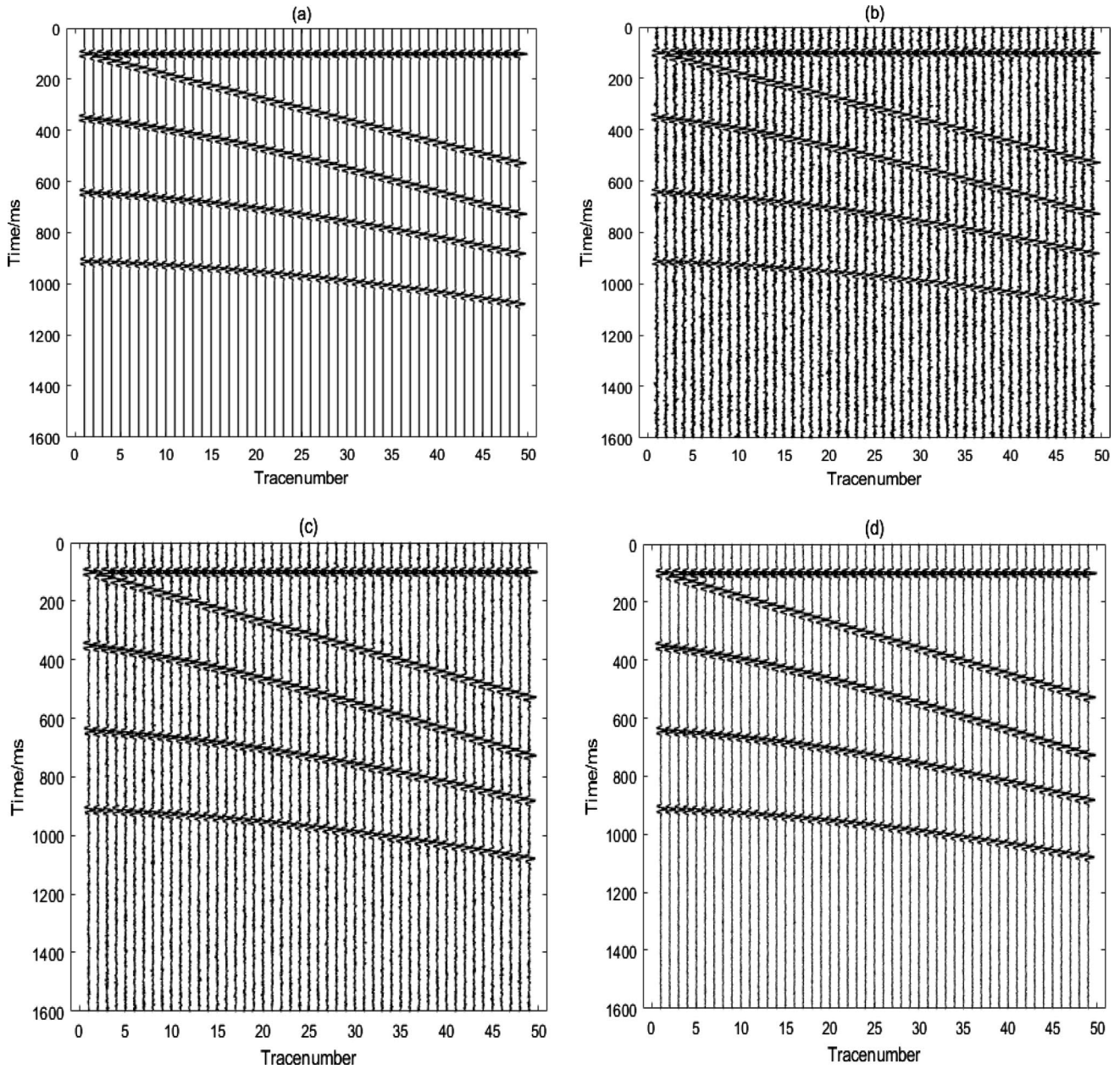


Fig. 8 a The synthetic seismic data; the noisy signal with the SNR of b 10 dB, c 20 dB, d 30 dB

The local fitness function f_j corresponds to the sequences before sorting and f_j^s is composed of f_j , which correspond to the elements of \mathbf{x}_j^s , rather than ascending sorting the elements of f_j .

To enhance calculation speed, this paper employs the following method to mutate the individual corresponding to f_j^s . By designating the variable corresponding to the local fitness function's minimum value as $x_{r,j}$, and randomly selecting two variables (excluding the minimum value) in the j th column of the population, the variation strategy for the j th element of the k th individual is:

$$x_{k,j}^M = x_{r,j} + F \cdot (x_{r1,j} - x_{r2,j}), \quad (23)$$

where F is a control parameter with a value that is a random variable between 0 and 1. All individuals undergo iteration to update genes in column j . The mutated genes are disturbed near the optimal value point, and the mutated values of different individuals slightly vary due to the distinct randomly selected variables and control parameters, which also align with nature laws and reflect mutation randomness.

Crossover operation: genes are randomly chosen from the target individual \mathbf{x}_i^G and its corresponding mutant individuals \mathbf{v}_i^G and combined into a test individual \mathbf{u}_i^G . The two commonly used crossover methods are uniform crossover and exponential crossover. We adopt the uniform crossover as follows:

$$u_{i,n}^G = \begin{cases} v_{i,n}^G & \text{if } r \leq \text{CR or } n = n_{\text{rand}}, \\ x_{i,n}^G & n = 1, 2, \dots, D, \end{cases} \quad (24)$$

where $\text{CR} \in [0, 1)$ is the crossover rate and n_{rand} is a random integer between 1 and D , ensuring that at least one of the genes in the test individual originates from the mutant individual.

Selection operation: the conventional selection operator selects an individual to advance to the next generation as a whole, according to the global fitness value of the target individual \mathbf{x}_i^G and the test individual \mathbf{u}_i^G , expressed as:

$$u_{i,j}^G = \begin{cases} u_{i,j}^s & \text{if } f_j(\mathbf{u}_{i,j}^G) \leq f_j(\mathbf{x}_{i,j}^G), \\ x_{i,j}^G & j = 1, 2, \dots, J, i = 1, 2, \dots, \text{NP} \end{cases} \quad (25)$$

In each iteration, we configured a support vector machine (SVM) classifier with a linear kernel using 90% of the training set and applied it to the remaining 10%. The SVM classifier is particularly suitable for binary classification problems, as it identifies an optimal separation hyperplane that maximizes the boundaries between classes. After training all samples once in the training set, we arrange the individuals in descending order according to their fitness values and retain only the top 10% of individuals. We generate the remaining 90% of new individuals by crossing over the randomly selected optimal individual pairs. Each new individual has a 10% chance of mutating (i.e., changing the code from 1 to 0 or from 0 to 1). We execute these iterative steps until all individuals are optimal and no further mutations occur. Finally, we select the filter corresponding to the position of the individual with the highest fitness value in the population.

Examples

Data set 1: synthetic seismic data with increasing SNR

We evaluate the noise resistance of the proposed method using a synthetic CMP record. Figure 8a displays the synthetic record with linear events and 3-layer nonlinear (hyperbolic) events. The source signature is a constant phase wavelet located at the surface with zero-offset, where $\sigma=50\text{Hz}$, $\delta=130$, $A'=1$, $\phi=0$. There are 100 geophones spaced 10 m apart. The sampling rate is 1 ms. The synthetic CMP record is augmented with white Gaussian noise, with the SNR ranging from 10–30 dB at intervals of 10 dB, as shown in Fig. 8b–d. The picked events are presented in Fig. 9a–c. As indicated by the solid ellipse in the images, as the SNR decreases, the precision of event extraction decreases and the events become discontinuous. However, when the SNR is high, the events picked up by the B-COSFIRE method remain relatively stable, indicating that the method has good noise resistance. Moreover, as highlighted by the dashed ellipse in Fig. 9a, this method can effectively separate thin layers. The filter system proves to be robust in noisy environments.

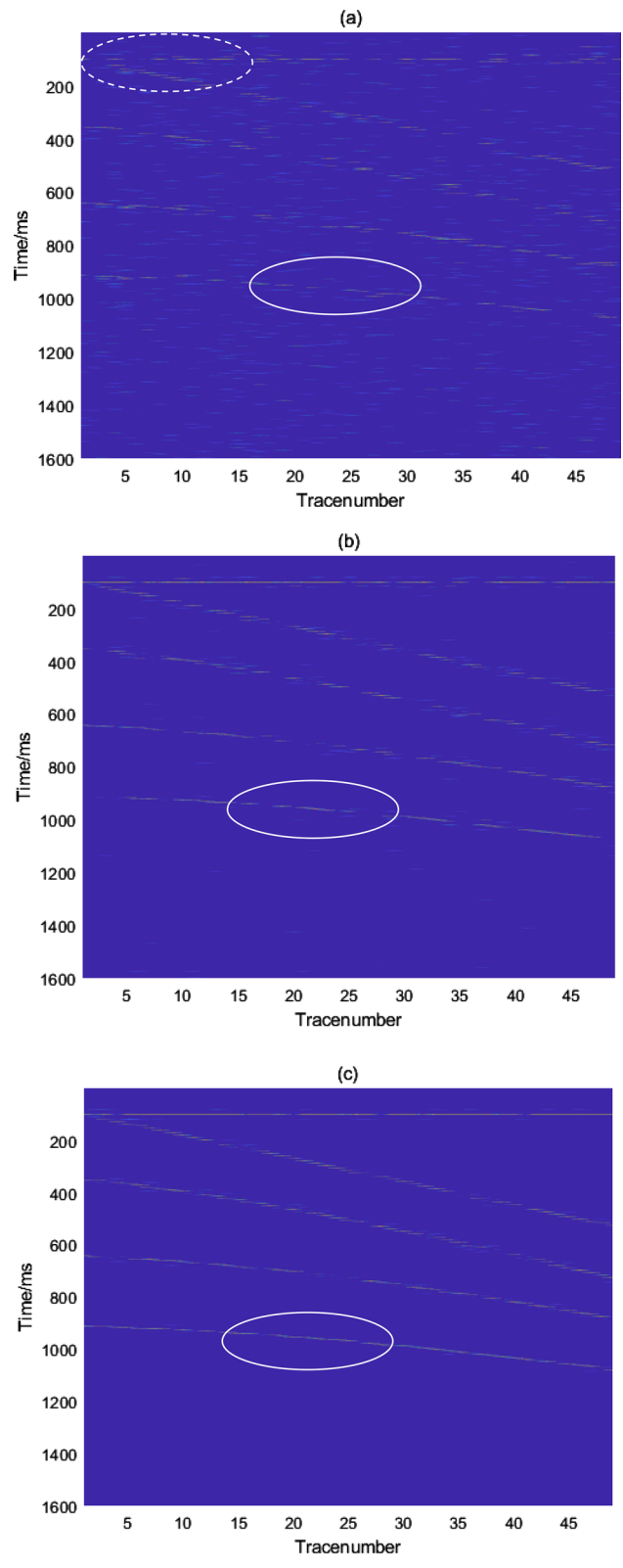


Fig. 9 Events picked up by the B-COSFIRE filter

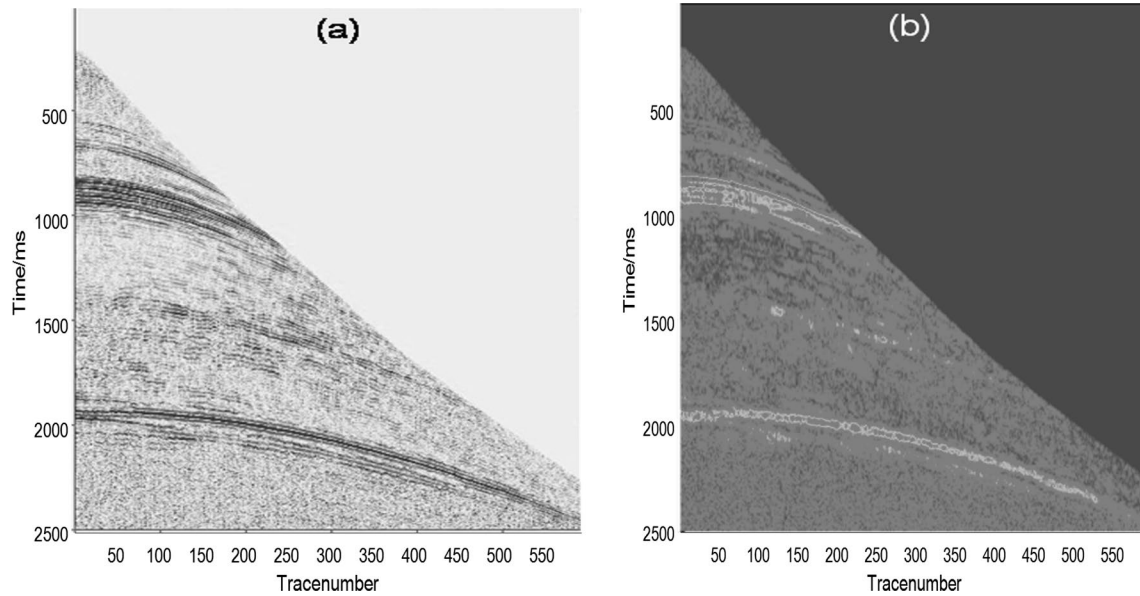


Fig. 10 Real seismic data. **a** Original pre-stack CSP data; **b** Instantaneous amplitude profile of **(a)**

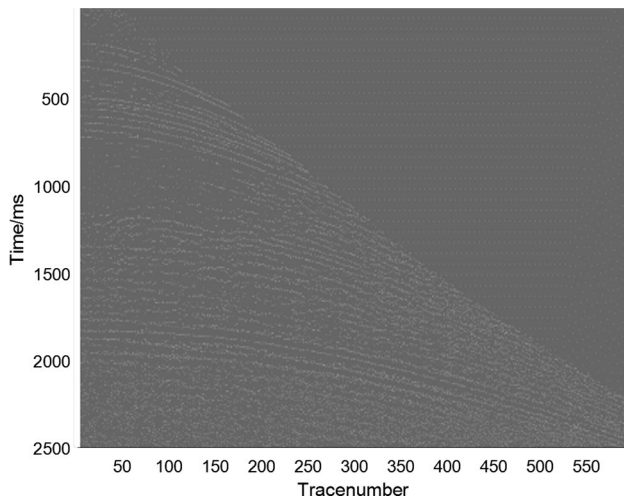


Fig. 11 Instantaneous frequency at the peak of the envelope

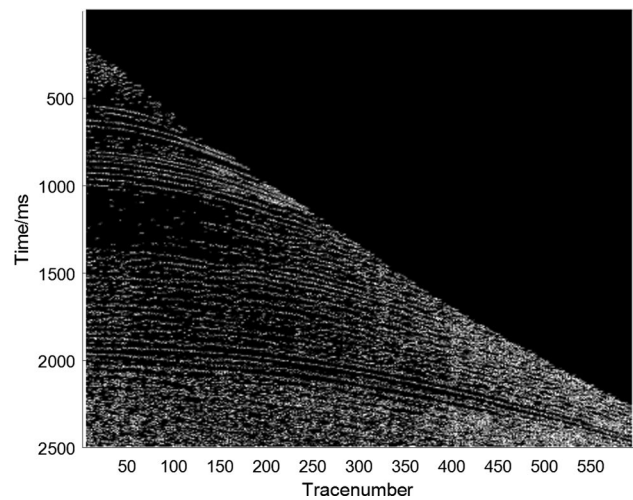


Fig. 12 Wavelet fusion profile of the instantaneous frequency of the envelope peak and the peak amplitude of the tilt superposition

Data set 2: real zero-offset VSP data

This paper applies the method to the real common shot point gather (CSP), which has 595 traces, 1250 sampling points, and 2-ms sampling interval. The minimum offset is 90 m, and the distance between the geophones is 10 m. Figure 10a displays the real pre-stack seismic data. The figure reveals that the original data have obvious events, but the background noise is substantial. In particular, the events at the near offset and shallow surface are indistinguishable. The peaks and troughs of the events interact, complicating dips and other attributes extractions. Figure 10b presents the instantaneous amplitude profile. Figure 11 displays the envelope peak instantaneous frequency (EPIF) profile, demonstrating that the envelope peak instantaneous frequency reduces peaks and troughs interference, concentrating effective information. However, deep medium noise remains significant. Figure 12 shows the wavelet fusion results of EPIF and the slant stack peak amplitude profile. The fused image emphasizes events and suppresses noise to a certain extent. Figure 13 illustrates the dip profile picked up by the Radon transform. Figure 14 presents the B-COSFIRE filter response. Figure 15 displays the events extraction results using the proposed method. Events extraction in the shallow layer is relatively complete. Thick strata events have been entirely picked up, and the noise marked by the ellipse has been significantly reduced, indicating the validity of the pro-posed method. Figure 16 shows

the result from the automatic events extraction method proposed by Zhao (2019). The auto events extraction method detects the upper and lower boundaries of each event (As indicated by the arrows), requiring human interaction for the final result. Figure 17 displays the non-maximum suppression result using the Canny operator. Figure 18 presents the events detection results using both Canny and Sobel operators. These results exhibit strong noise and disturbance, with the events being less complete compared to those obtained with the B-COSFIRE method. By comparing Fig. 15 with Figs. 16, 17 and 18, it is evident that the events picked up by the B-COSFIRE method are more complete and more continuous, demonstrating good noise resistance.

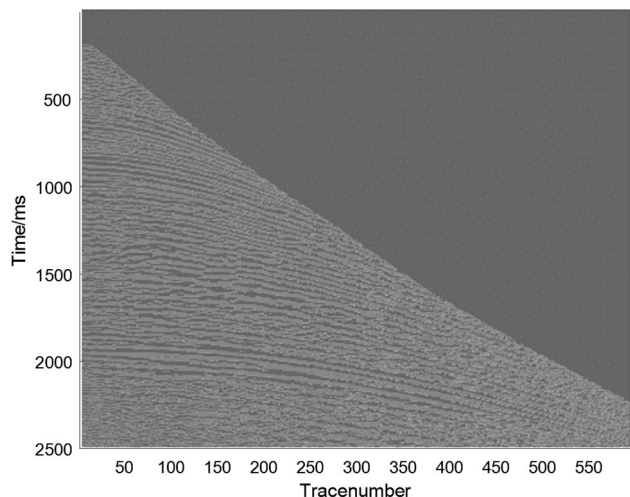


Fig. 13 Dip profile obtained by Radon transform

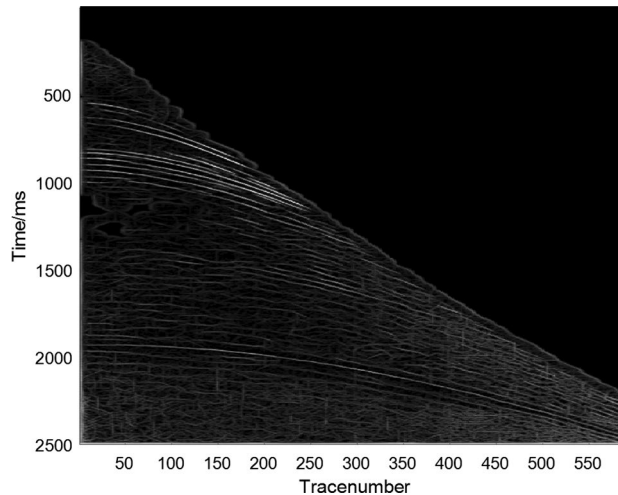


Fig. 14 Response result of the B-COSFIRE filter

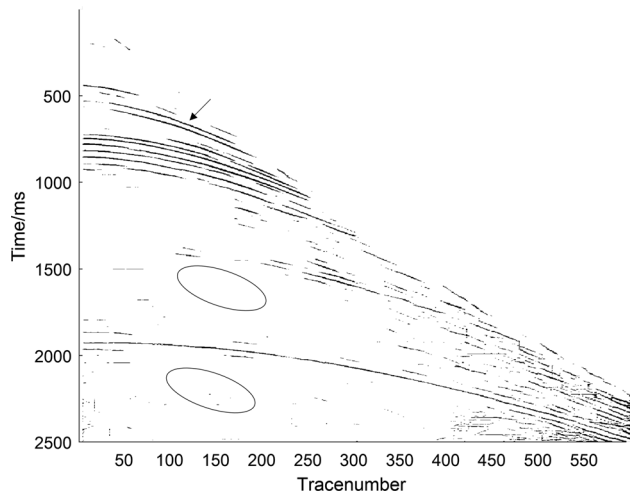


Fig. 15 Events picked up by the B-COSFIRE filter

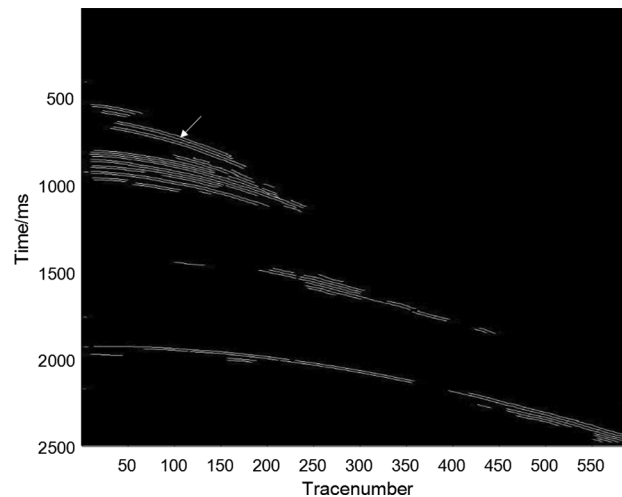


Fig. 16 The result of the automatic events extraction method

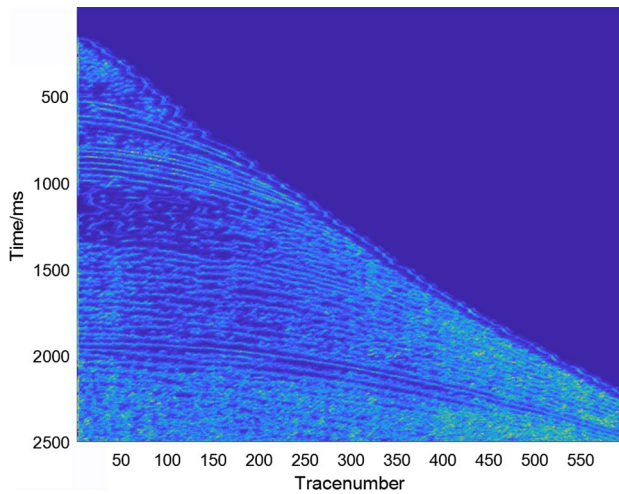


Fig. 17 Events detection result by Canny operator

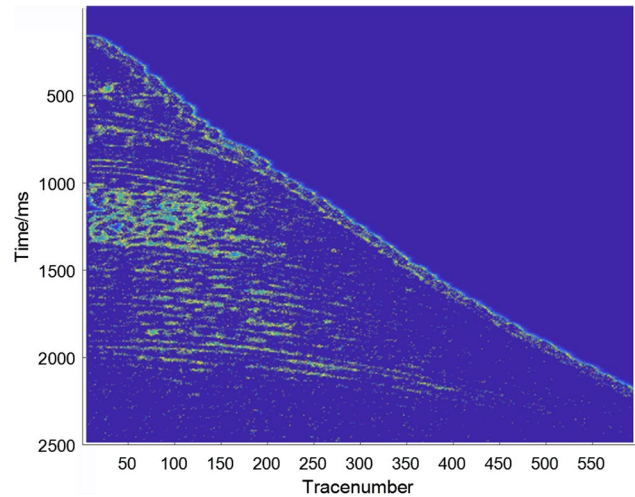


Fig. 18 Events detection result by Canny and Sobel operator

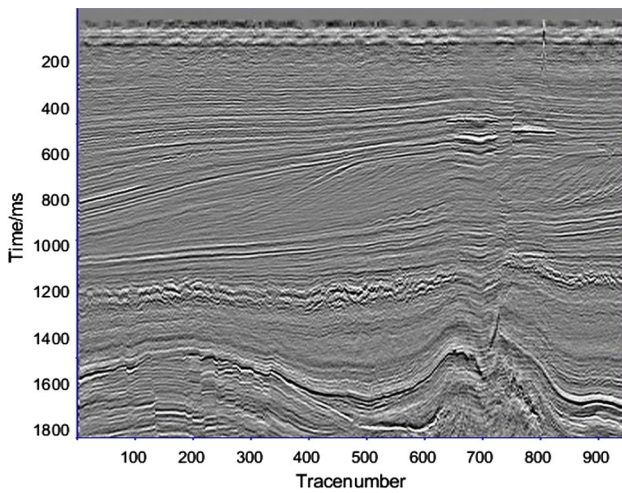


Fig. 19 A 2D section of F3 block (North seas)

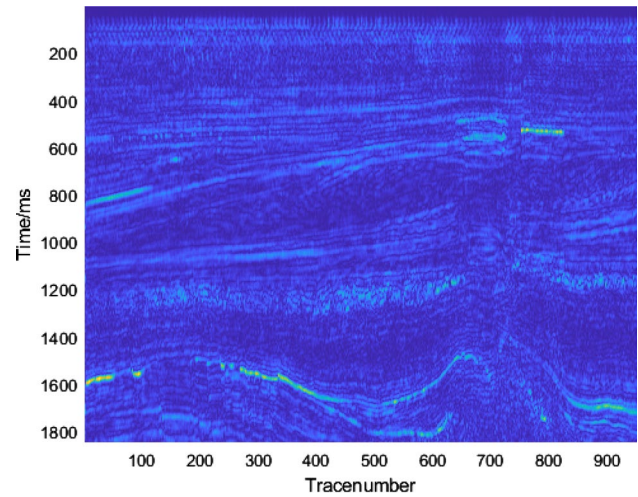


Fig. 20 Instantaneous amplitude (IA) profile of F3 block (North seas)

Data set 3: 2D section of F3 block (North seas)

We applied the method to the F3 block of the North Sea data (Fig. 19) to identify horizons in stacked sections with faults or folding. Figure 20 displays the instantaneous amplitude (IA) profile of the F3 block. Figure 21 is the instantaneous frequency (IF) result of the F3 block. Figure 22 shows the envelope peak instantaneous frequency (EPIF) section. Figure 23 presents the response result of the B-COSFIRE filter. Figure 24 presents the events detection result for the F3 block. The extracted events and folding appear complete, and the noise has been significantly reduced, demonstrating the effectiveness of the proposed method.

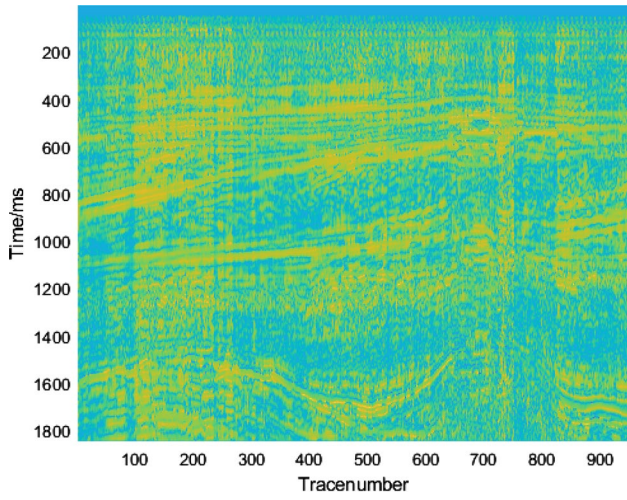


Fig. 21 Instantaneous frequency (IF) profile of F3 block (North seas)

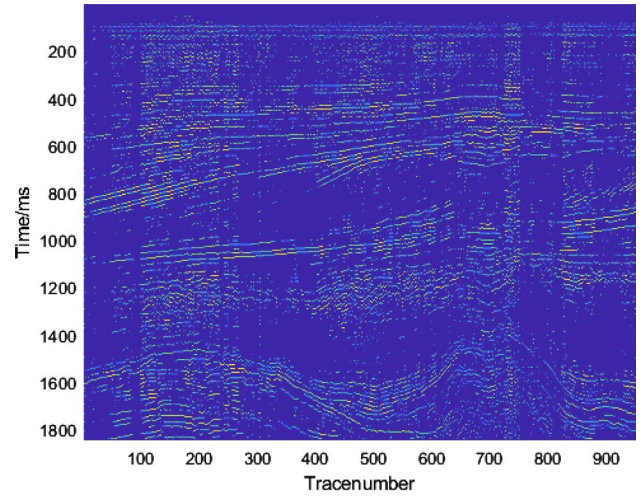


Fig. 22 EPIF profile of F3 block (North seas)

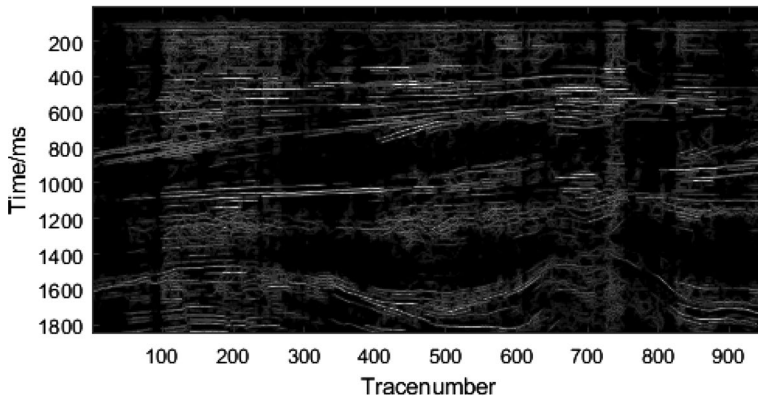


Fig. 23 The Response result of the B-COSFIRE filter for F3 block

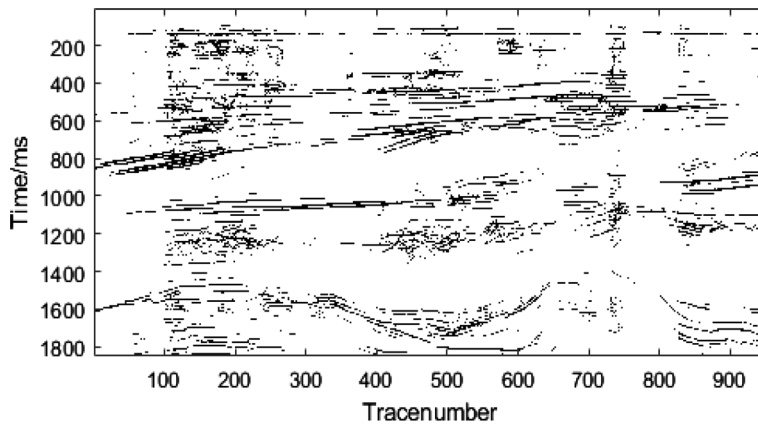


Fig. 24 The Events detection result of F3 block

Conclusions

This paper introduces a seismic events extraction method based on the B-COSFIRE filter combined with the differential evolution algorithm. In this approach, each sampling point is described by two values—one from the bar structure selection filter, and the other from the bar structure end selection filter—both of which are merged through summation. This combination enhances the response to the bar structure and its endpoints, thereby improving the extraction ability of events and increasing extraction accuracy. The B-COSFIRE filter proposed in this paper is a trainable filter, as its selectivity is not predefined upon implementation but is determined by the user-specified prototype pattern during the automatic configuration process. The filter's optimal parameters are automatically configured according to the target, ultimately yielding optimal extraction results. The weighted geometric mean used in this paper is a nonlinear function that produces a response only when all the filters for points of interest are present. This means it cannot generate a response at discontinuities, which enhances the continuous effective signal and weakens the discontinuous noise signal, making this type of function more robust to noise than other methods. The method can automatically select bar structures with different widths using the differential evolution algorithm, evaluate the combined contribution of numerous features, and explore a larger solution space. The seismic data used by this algorithm is in 'sgy' format, which contains abundant information. In accordance with the unique visual cognition method applied in the seismic field, we do not convert the seismic data into grayscale images but instead use the data itself. More attribute information can be extracted from the data, such as instantaneous frequency and instantaneous amplitude, to perform event extraction. We maximize the resolution and retain the information. The proposed method demonstrates high flexibility and can pick up events with different widths. The target's contour within the events is well extracted, and the extraction results can be applied to the subsequent seismic interpretation and reservoir prediction.

Acknowledgements The authors are thankful to the reviewers for their useful suggestions.

Funding This work is partially supported by the Natural Science Foundation of Shaanxi Province, China (2021JQ-587), National Natural Science Foundation of China (41604113), National Nature Science Foundation Project of International Cooperation (41711530128), Key research and development projects in Shaanxi Province (2022GY-148). We also thank Changqing oilfield for their field data.

Declarations

Conflict of interest On behalf of all authors, the corresponding author states that there is no conflict of interest.

References

- Arrowsmith SJ, Eisner L (2006) A technique for identifying micro-seismic multiplets and application to the Valhall field, North Sea. *Geophys J Int* 71(2):V31–V40
- Azzopardi G, Petkov N (2012) A CORF computational model of a simple cell that relies on LGN input outperforms the Gabor function model. *Biol Cybern* 106:177–189
- Azzopardi G, Petkov N (2013) Trainable COSFIRE filters for keypoint detection and pattern recognition. *IEEE Trans Pattern Anal Mach Intell* 35(2):490–503
- Azzopardi G, Strisciuglio N, Vento M, Petkov N (2015) Trainable cosfire filters for vessel delineation with application to retinal images. *Med Image Anal* 19(1):46–57. <https://doi.org/10.1016/j.media.2014.08.002>
- Badawi SA, Fraz MM (2018) Optimizing the trainable B-COSFIRE filter for retinal blood vessel segmentation. *PeerJ*. <https://doi.org/10.7717/peerj.5855>
- Bondar I (1992) Seismic horizon detection using image processing algorithms. *Geophys Process* 40(7):785–800. <https://doi.org/10.1111/j.1365-2478.1992.tb00552.x>
- Chen Y (2020) Automatic microseismic event picking via unsupervised machine learning. *Geophys J Int* 222(3):1750–1764. <https://doi.org/10.1093/gji/ggaa186>
- Ding WH, Pan GH, Gou ZH, Fu XM, Zhang JB, Hu TJ (2012) The research of interactive auto pickup of seismic events based on energy ratio and cross-correlation. *Acta Oceanol Sin* 34(3):87–91. <https://doi.org/10.1007/s11783-011-0280-z>
- Gao JH, Yang S, Wang D et al (2011) Estimation of quality factor Q from the instantaneous frequency at the envelope peak of a seismic signal. *J Comput Acoust* 19(02):155–179
- Gibbons SJ, Ringdal F (2006a) The detection of low magnitude seismic events using array-based waveform correlation. *Geophys J Int* 165(1):149–166. <https://doi.org/10.1111/j.1365-246X.2006.02865.x>
- Gibbons SJ, Ringdal F, Kvaerna T (2006b) Detection and characterization of seismic phases using continuous spectral estimation on incoherent and partially coherent arrays. *Geophys J Int* 172(1):405–421. <https://doi.org/10.1111/j.1365-246X.2007.03650.x>

- Glinsky ME (1991) Automatic event picking in prestack migrated gathers using a probabilistic neural network. *Geophysics* 66(5):1488–1496. <https://doi.org/10.1190/1.1487094>
- Haralick RM (1984) Digital step edges from zero crossing of second directional derivatives. *IEEE Trans Pattern Anal Mach Intel PAMI* 6(1):58–68. <https://doi.org/10.1109/TPAMI.1984.4767475>
- Irvine G, Casagrande V, Norton T (1993) Center surround relationships of magnocellular, parvocellular, and koniocellular relay cells in primate lateral geniculate-nucleus. *Vis Neurosci* 10:363–373
- Lara MD, Kristian G, George A (2019) Age group recognition from face images using a fusion of CNN- and COSFIRE-based features. In: *Proceedings of the 2nd International conference on applications of intelligent systems (APPIS '19)*. <https://doi.org/10.1145/3309772.3309784>
- Li HX, Liu C, Tao CH (2007) The study of application of edge measuring technique to the detection of phase axis of the seismic section. *Prog Geophys* 22(5):1607–1610. [https://doi.org/10.1016/S1872-5791\(08\)60015-9](https://doi.org/10.1016/S1872-5791(08)60015-9)
- Li X (2015) Automatic seismic event pickup using edge measuring technique. Ocean University of China
- Liu N, Chen J, Wu H, Li F, Gao J (2022) Microseismic first-arrival picking using fine-tuning feature pyramid networks. *IEEE Geo-sci Remote Sens Lett* 19:1–5
- Lu JM (1993) Principles of seismic exploration. China University of Petroleum Press, Qingdao
- Ma P, Ren J, Sun G, Zhao H, Jia X, Yan Y, Zabalza J (2023) Multiscale superpixelwise prophet model for noise-robust feature extraction in hyperspectral images. *IEEE Transact Geosci Remote Sens* 61:1–12. <https://doi.org/10.1109/TGRS.2023.3260634>
- McComack MD (1993) First-break refraction event picking and seismic data trace editing using neural network. *Geophysics* 58(1):67. <https://doi.org/10.1190/1.1443352>
- Michelet S, Toksöz MN (2007) Fracture mapping in the Soultz-sous-forets geothermal field using microearthquake locations. *J Geo-phys Res* 112:B07315. <https://doi.org/10.1029/2006J B004442>
- Ning JS, Wang HH, Luo ZC (2015) Downward continuation of gravity signals based on the multiscale edge constraint. *Chin J Geophys* 48(1):63–68. <https://doi.org/10.3321/j.issn:0001-5733.2005.01.011>. (in Chinese)
- Rodieck RW (1965) Quantitative analysis of cat retinal ganglion cell response to visual stimuli. *Vis Res* 5:583–601
- Schultz R, Yu Jeffrey Gu (2013) Flexible, inversion-based Mat-lab implementation of the Radon transform. *Comput Geosci* 52:437–442
- Song F, Toksöz MN (2011) Full-waveform based complete moment tensor inversion and source parameter estimation from downhole microseismic data for hydrofracture monitoring. *Geophysics* 76(6):WC103–WC116. <https://doi.org/10.1190/geo2011-0027.1>
- Song F, Kuleli HS, Toksöz MN, Ay E, Zhang H (2010) An improved method for hydrofracture-induced microseismic event detection and phase picking. *Geophysics* 75(6):A47–A52. <https://doi.org/10.1190/1.3484716>
- Spagnolini U (1991) Adaptive picking of refracted first arrivals. *Geo-phy Prosp* 39(3):293–312. <https://doi.org/10.1111/j.1365-2478.1991.tb00314.x>
- Strisciuglio N, Azzopardi G, Vento M, Petkov N (2016) Supervised vessel delineation in retinal fundus images with the automatic selection of b-cosfire filters. *Mach vis Appl* 27(8):1137–1149. <https://doi.org/10.1007/s00138-016-0781-7>
- Strisciuglio N, Petkov N (2017) Delineation of line patterns in images using B-COSFIRE filters. In: *International conference and work-shop on bioinspired intelligence (IWObI)*. doi:<https://doi.org/10.1109/iwobi.2017.7985538>
- Strisciuglio N, Azzopardi G, Petkov N (2017) Detection of curved lines with b-cosfire filters: a case study on crack delineation. In: *International conference on computer analysis of images and pat-terns*. *Cham*. pp. 108–120.
- Tu P, Mason I, Zisserman A (1993) An automated system for picking seismic events. *SEG 63rd annual meeting, 1993*. pp 234–237
- Wang C, Gao JH (2012) High-dimensional waveform inversion with cooperative coevolutionary differential evolution algorithm. *IEEE Geosci Remote Sens Lett* 9:297–301. <https://doi.org/10.1109/LGRS.2011.2166532>
- Wang Z, Ren JC, Zhang D, Sun M, Jiang J (2018) A deep-learning based feature hybrid framework for spatiotemporal saliency detection inside videos. *Neurocomputing* 287:68–83. <https://doi.org/10.1016/j.neucom.2018.01.076>
- Wang C, Gao JH (2010a) A new differential evolution algorithm with cooperative coevolutionary selection operator for waveform inversion. *IEEE International Geoscience and Remote Sensing Symposium (IGARSS)*. pp 688–690. <https://doi.org/10.1109/igarss.2010.5652032>
- Wang C, Gao J (2010b) A new differential evolution algorithm with cooperative coevolutionary selection operator for waveform inversion. In: *IEEE*. 2010. pp 688–690
- Xiong HJ, Guan YP, Yu YJ (2009) Extraction of cophasal axes on seismic sections based on the edge detection method. *Prog Geophys* 24(6):2250–2254. <https://doi.org/10.3969/j.issn.1004-2903.2009.06.045>. (in Chinese)
- Xu X, Bonds A, Casagrande V (2002) Modeling receptive-field structure of koniocellular, magnocellular, and parvocellular LGN cells in the owl monkey (*Aotus trivigatus*). *Visual Neurosci* 19:703–711
- Zhao J, Gao JH, Wang DX, Zhang ML (2013) Q-factor and velocity inversion from zero-offset VSP data. *J Appl Geophys* 101:51–67
- Zhao J, Ren JC, Gao JH, Tschannerl J, Murray P, Wang DX (2019) Automatic events extraction in pre-stack seismic data based on edge detection in slant-stacked peak amplitude profiles. *J Petrol Sci Eng* 178:459–466. <https://doi.org/10.1016/j.petrol.2019.03.062>
- Zhao H (2005) The layer tracking of fault's sides based on the artificial neural networks. Chengdu University of Technology.
- Zhou YJ, Yue H, Kong QK, Zhou SY (2019) Hybrid event detection and phase-picking algorithm using convolutional and recurrent neural networks. *Seismol Res Lett* 90:1079–1087. <https://doi.org/10.1785/0220180319>
- Zhu WB, Li B, Tian LF, Li XX, Chen QL (2015) Topology adaptive vessel network skeleton extraction with novel medialness measuring function. *Comput Biol Med* 64:40–61. <https://doi.org/10.1016/j.combiomed.2015.06.006>